Estimation of Speed of Sound in Dual-Layered Media using Medical Ultrasound Image Deconvolution

Ho-Chul Shin, Richard Prager, Henry Gomersall,
Nick Kingsbury, Graham Treece and Andrew Gee

*Department of Engineering, University of Cambridge,
Trumpington Street, Cambridge, CB2 1PZ, United Kingdom*

Abstract

The speed of sound in soft tissues is assumed as 1540 m/s in medical pulse-echo ultrasound imaging systems. When the true speed is different, the mismatch can lead to distortions in the acquired images, and so reduce their clinical value. Previously we reported a new method of sound-speed estimation in the context of image deconvolution. This enables the use of unmodified ultrasound machines and a normal scanning pattern unlike most other sound-speed estimation methods. Our approach was validated for largely homogeneous media with single sound speeds. In this article, as an extension to the aforementioned algorithm, we demonstrate that sound speeds of dual-layered media can also be estimated through image deconvolution. An ultrasound simulator has been developed for layered media assuming that, for moderate speed differences, the reflection at the interface may be neglected. We have applied our dual-layer algorithm to simulations and *in vitro* phantoms. The speed of the top layer is estimated by our aforesaid method for a single speed. Then, when the layer boundary position is known, a series of deconvolutions are carried out with dual-layered PSFs having different lower-layer speeds. The best restoration is selected using a correlation metric. The error level for *in vitro* phantoms is found to be not as good as that of our single-speed algorithm, but is comparable to other local speed estimation methods.

Keywords: Medical ultrasound image; Dual-layered media; Non-blind deconvolution; Point-spread function; Speed of sound; Sound estimation.

1 Introduction

Pulse-echo medical ultrasound imaging assumes the speed of sound is 1540 m/s in soft tissue for the beamforming delay profile and the display of acquired images. The current convention of using the assumed speed potentially leads to distortions in B-mode images when the actual speed of sound is different. The effects of errors in the sound speed, such as degraded spatial resolution, have been widely reported, and some of the consequences have been quantified [1]. Therefore, the estimation of the correct acoustic speed is beneficial in improving the overall image quality and hence in increasing its diagnostic value. At the same time, the estimated speed of sound itself has its own significance in the context of tissue characterisation.

Initially, the speed of medical ultrasound was estimated using transmission methods, which measured the time taken while a pulse propagated between a transmitter and a receiver. But clinical applications were limited to the breast [2]. Robinson et al. [3] carried out an extensive review of pulse-echo sound-speed estimation techniques. Nine methods in three categories were examined in detail. Most of the reviewed methods produce the average speed of sound in the scanned tissues. Only a few were capable of local speed estimation. Kondo et al. [4] reported the estimation of *in vivo* local speed of sound. But, they also stated that an exact measurement of local sound speed was difficult. Ophir and Yazdi [5] applied transaxial compression technique to a dual-layered *in vitro* phantom made of polyester sponge, water and glycol solution. The technique can be carried out by a single transducer, but this is often accompanied by a second transducer to compensate for potential movement of the region of interest caused by compression of the phantom surface.

Recently, a detailed local sound-speed estimation of biological tissue was demonstrated using ultrasound based on a scanning acoustic microscope (SAM) [6] and a computed tomography (CT) [7, 8, 9, 10, 11]. However, these methods using either SAM or CT technologies are effectively different modalities from that with which we are concerned. The signal carrier frequency of SAM system reaches as high as 500 MHz, and as in other microscope techniques non-invasive measurement is not possible. The CT systems have been demonstrated in a recent pre-clinical trial [11] to be capable of the detailed estimation of sound speed as well as attenuation. However, its transmissional use of ultrasound is limited to breast imaging. It is also different from the pulse-echo approach addressed in this paper and requires higher system complexity like other CT systems.

The correction of wrong sound-speed effects, especially due to tissue inhomogeneity, has been addressed in the context of phase aberration [12]. Numerous methods have been proposed [13, 14, 15, 16]. They may differ from one another in how the aberration profiles are estimated across the transducer elements, but many of them share the idea of changing the time delays in individual elements according to the estimated aberration profile. During the profile estimation process, many techniques require multiple acquisitions of the radio-frequency (RF) signal. Most of all, previous works on phase aberration have concentrated on the reduction of perceived image degradation.

Our research group has recently published a novel speed-of-sound estimation technique by using image deconvolution [17]. The algorithm is based on the assumption that soft tissue is mainly homogeneous and its underlying speed of sound is constant. Our published technique has several advantages over other methods of medical ultrasound speed estimation reported by others [3]. The data can be collected by a single scan using a single transducer array unlike other methods [2, 3, 18]. No transducer movement is required, whereas precise movement is commonplace in other techniques [3, 5]. No special rigs are necessary in holding the transducer to satisfy a geometric constraint inherent as in some other methods [3, 19]. In other words, conventional use of a linear transducer array is sufficient in the data acquisition aspect of our algorithm.

The fundamental concept enabling the speed estimation in our method is image deconvolution [20, 21, 22]. The power of using non-blind deconvolution is that we do not need multiple ultrasound scans, as some other methods do in order to adjust their beamforming time delays [3, 18].

Necessary variations can be easily accomplished off-line by adjusting the PSF in our deconvolution framework, where the PSFs are calculated by using the Field-II program [23].

However, our original approach was not capable of handling inhomogeneous tissues. As an idealised scenario of non-uniform soft tissue, we now consider a layered medium formed of two layers with different sound speeds. We demonstrate that image deconvolution can be used to estimate sound speed in such an environment.

The rest of the paper is arranged into the following sections: Section 2 describes the modelling of ultrasound behaviour in dual-layered media. Section 3 explains the development of an ultrasound simulator applicable to layered media. Section 4 presents the result of the simulations together with the method of estimating the speed. Section 5 addresses the speed estimation of *in vitro* phantoms. Finally, conclusions are drawn and followed by a brief introduction of our non-blind deconvolution algorithm in Appendix A.

2 Medical ultrasound in dual-layered soft tissue

An acoustic wave, of which an ultrasound wave may be considered a subset, is reflected and transmitted when it encounters the boundary between different media. In general, the phenomenon of transmission is complicated. However, the situation can be eased when the acoustic wave front and the medium boundary are planar and the involved media are all considered as a fluid rather than a solid (p.124 in [24]).

Here, we define a fluid as a medium where propagation of a longitudinal wave is dominant but a transverse wave is discouraged, whereas a solid as a medium in which both forms of waves are free to propagate. In fluids the path of refracted waves is easily determined by the refraction index, but solids are often anisotropic and hence the direction of a transmitted wave is influenced by local structure.

In soft tissue, transverse waves have a low propagation speed of around 100 m/s. They are severely attenuated at frequencies over 1 MHz and can therefore be neglected (p.1.4 in [25]). Also in their composition, soft tissues are mainly made of water with a few solid components added. Therefore, in diagnostic medical ultrasound imaging, soft tissues can be treated as a fluid.

2.1 Reflection in dual-layered soft tissues

It is widely known that most ultrasound energy at normal incidence is transmitted with negligible loss of reflection at the boundary of different types of soft tissues (see Table 1-8 in [25]). But for ultrasound probes consisting of arrays of piezoelectric elements, oblique incidence does occur regardless of transducer positioning. For oblique incidence, the power reflection coefficient $\mathbf{R}$ at the fluid-fluid boundary is given by (see p.132 [24]):

$$\mathbf{R} = \left| \frac{(\rho_2/\rho_1)\ c_2/c_1 \ - \ \cos\theta_2/\cos\theta_1}{(\rho_2/\rho_1)\ c_2/c_1 \ + \ \cos\theta_2/\cos\theta_1} \right|^2 . \tag{1}$$

Here, the symbols ρ, c and θ indicate density, sound speed and angle, respectively. The subscripts 1 and 2 denote the layers 1 and 2. Equation 1 is valid when the angle θ_2 is real, otherwise the coefficient $\mathbf{R}$ is unity. The refracted angle θ_2 becomes complex when the incident angle θ_1 is bigger than a critical angle determined by the ratio of both speeds of sound.

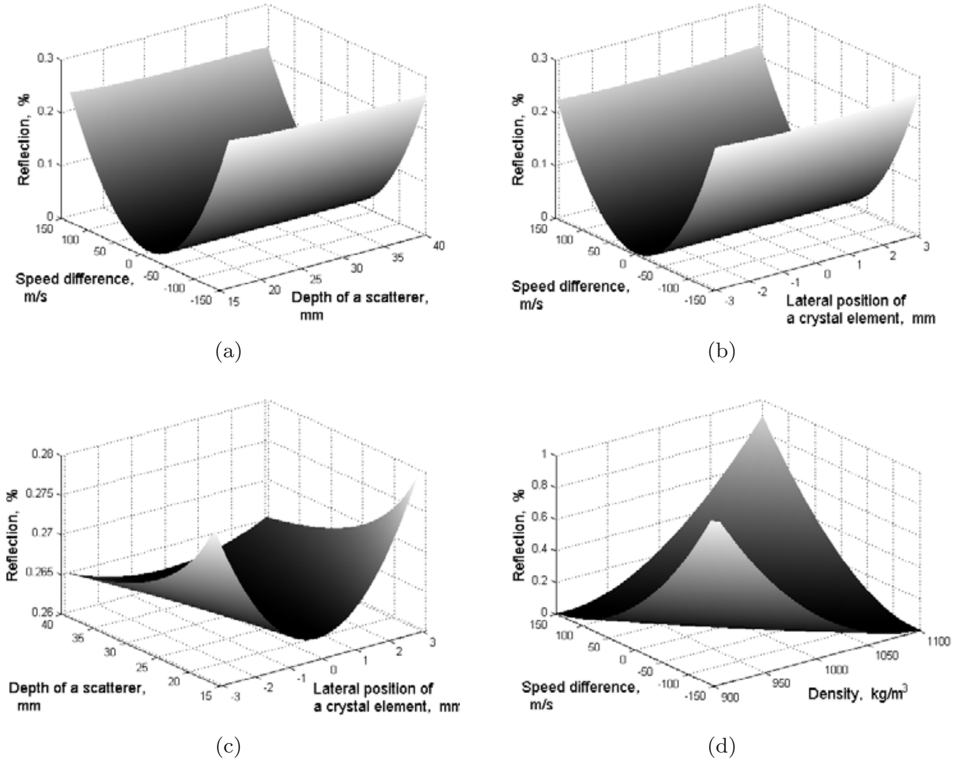

Figure 1: Power reflection coefficient **R** at a boundary depth of 16 mm. Subplot (a) shows R as a function of the speed difference between layers and of scatterer depth, for a crystal element located at -3.0535 mm with a layer-2 density of 1000 kg/m^3. Subplot (b) shows R as a function of the speed difference between layers and of crystal element position, for a scatterer depth of 25 mm with a layer-2 density of 1000 kg/m^3. Subplot (c) shows R as a function of scatterer depth and of crystal element position, for a speed difference of -150 m/s with a layer-2 density of 1000 kg/m^3. Subplot (d) shows R as a function of the speed difference between layers and of layer-2 density, for a crystal element located at -3.0535 mm and a scatterer depth of 25 mm. Note the coefficient is displayed as a percentage.

Examples of the power reflection coefficient **R** relevant to one of our ultrasound probes are shown in Figure 1. The ultrasound probe has 32 active piezoelectric elements whose geometric centres are laterally spread from -3.0535 to +3.0535 mm with an interval of 0.197 mm. Speed differences, $c_2 - c_1$, were investigated in the range from -150 to +150 m/s when $c_1 = 1540$ m/s. The sound speed of most biological materials except bone falls well within the range: the lower end of fat being 1440 m/s; the higher end of muscle at 1626 m/s (see Table 1-1 in [25]). Note that quoted values may be slightly different depending on the source of information. The density of layer 1 was chosen as 1000 kg/m^3, which is equivalent to that of water. The density of layer 2 was varied from 900 to 1100 kg/m^3, which covers most forms of soft tissues: from 950 kg/m^3 for fat to 1070 kg/m^3 for muscle (see Table 1-1 in [25]). The depth of a scatterer in the bottom layer is varied from 16.1 to 40.0 mm when the boundary is located at a depth of 16 mm.

These graphs show that the coefficient is mostly affected by differences in speed and density, and also imply that the extra effect of oblique incidence is not significant. In general the amount of the reflection is very low. Only the extreme combinations of sound speed and density see the reflection reach 1 % of the incident energy. We are therefore reassured that most of ultrasound

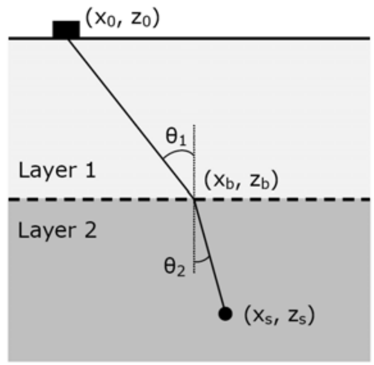

Figure 2: Schematic diagram showing the geometric relationship between incident and refracted ultrasound waves in a fluid. The position of the transmit or receive crystal element is denoted by (x_0, z_0), that of the scatterer by (x_s, z_s), and that of the interaction point at the boundary by (x_b, z_b). All three of these points are assumed to be in a plane and to have the same y-coordinate. The medium boundary is assumed to be parallel to the transducer aperture of a linear array

energy are transmitted and hence the reflection can be ignored.

This assumption of the reflection being ignored not only simplifies the ultrasound image formation for the bottom layer but also validates the use of deconvolution in the top layer. Our deconvolution algorithm like many other linear deconvolution models assumes the first-order Born approximation, which results in the sonification of scatterers by waves directly from transducer elements. Therefore, strong reflections at the boundary could generate secondary sources which would reduce the accuracy of our deconvolution in the top-layer part of the media.

Because of its importance in our estimation method, for readers who may not be familiar with ultrasound image deconvolution, our non-blind deconvolution algorithm is briefly introduced in Appendix A. Complete details can be found in previous publications [20, 21].

2.2 Refraction in dual-layered media

In creating PSFs with dual-layer characteristics, the determination of an interaction point along the boundary is of paramount importance. Its location will decide the difference between the refracted path of the ultrasound and the straight path as if there were only a single homogeneous layer between the scatterer and the piezoelectric element. This difference in distance and subsequently in arrival time will generate an overall perception of B-mode image distortion when soft tissue is composed of layers with different speeds of sound.

When both media at the boundary are isotropic such as fluid, the well-known Snell's law may be applied to establish the relationship between the speeds in the adjacent media and the angles of incidence and refraction of plane waves (p.131 in [24]):

$$\frac{\sin\theta_1}{c_1} = \frac{\sin\theta_2}{c_2}\,. \tag{2}$$

The geometric relationship is shown in Figure 2. Each layer is assumed to be macroscopically homogeneous and isotropic, and hence to have uniform macroscopic properties. But the media may be considered microscopically inhomogeneous enough to have back scattering from the ultrasound. The position of the transmit or receive crystal element is denoted by (x_0, z_0), that of the scatterer by (x_s, z_s), and that of the interaction point at the boundary by (x_b, z_b). All three pairs of points are assumed to be in a plane and to have the same y-coordinate. This constraint can be easily met by a coordinate transformation. The medium boundary is assumed to be semi-infinite and parallel to the transducer aperture of a linear array. Since our deconvolution algorithm like others assumes shift invariance in the lateral dimension of the probe, the medium boundary and the probe surface are required to be parallel each other. Layer 1 is designated to have a uniform sound speed of c_1 and layer 2 to have c_2. The incidence and refraction angles on the boundary are denoted by θ_1 and θ_2, respectively. When the trigonometric rule is applied to Snell's law, the squared version of Eq. 2 becomes:

$$\frac{1}{c_1^2}\frac{(x_b-x_0)^2}{(z_b-z_0)^2+(x_b-x_0)^2}=\frac{1}{c_2^2}\frac{(x_s-x_1)^2}{(z_s-z_1)^2+(x_s-x_1)^2}\ . \tag{3}$$

In our problem formulation, every variables in Eq. 3 apart from the lateral location on the boundary (x_b) are assumed to be known including the depth of the boundary (z_b). A few steps of simple arithmetic from Eq. 3 lead to the following quartic equation:

$$p_4\,x_b^4+p_3\,x_b^3+p_2\,x_b^2+p_1\,x_b+p_0=0\ . \tag{4}$$

where coefficients are arranged as follows, and the simplest scenario is assumed in which the crystal element is placed at the origin of the coordinate system $(x_0 = 0,\ z_0 = 0)$, which is also easily achieved by the translation of a coordinate system:

$$p_4 = 1-\delta^2\ ;$$

$$\delta = c_1\,/\,c_2\ ;$$

$$p_3 = 2\,x_s\,p_4\ ;$$

$$p_2 = (z_s-z_1)^2+x_s^2-\delta^2(z_1^2+x_s^2)\ ;$$

$$p_1 = -2\,x_s\,z_1^2\,\delta^2\ ;$$

$$p_0 = -\,\delta^2\,z_1^2\,x_s^2\ .$$

The quartic equation can be easily solved for example via Matlab command *roots.m*, and lead to a single unique solution of x_b through the constraint of it being real and positioned between the transducer element and the scatterer in question. The concept for the dual-layer situation can be easily extended to media with more than two layers, but the solution will involve a system of quartic equations.

3 Dual-layer ultrasound simulator

Dual-layered media may be simulated in principle by modifying the outputs of the Field-II program [23]. For the top layer, the conventional use of the program is sufficient. For the bottom layer, its raw outputs, which do not involve any apodisation and focusing, are first obtained for every combination of transmit and receive elements in the aperture. Then, differences of transmission paths due to refraction calculated in Section 2.2 are applied to adjust beamforming delay profiles across the transducer aperture. The process may be regarded as a form of aperture synthesis.

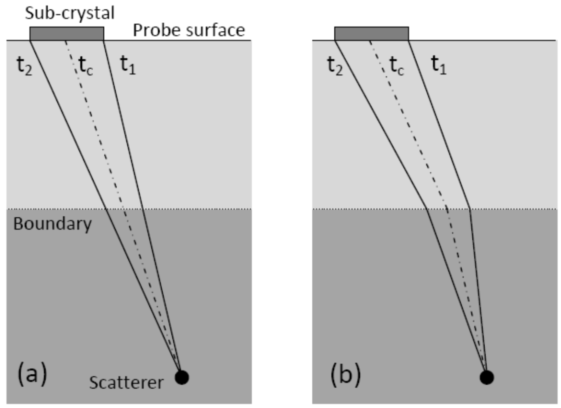

Figure 3: Schematic diagram showing spatial impulse response of transducer elements. Subplot (a) is what happens using Field-II outputs. Subplot (b) is what may happen in a dual-layer medium.

Although we are able to conduct such delay modification to generate the effect of a dual-layered medium, what we may not adjust is the way each "finite" transducer element responds to outgoing and incoming ultrasound signals (or the diffraction pattern occurring at the element). Figure 3 illustrates the situation, which is an idealised case of two-dimensional interaction for brevity. Subplot (a) corresponds to an ordinary run of Field-II. "Sub-crystal" means that each individual crystal is divided into a collection of smaller areas. This sub-division is required mainly for two reasons. The first is that the elements should be divided at least in the elevational dimension in order to simulate an elevational focus. The second and more important reason is to make the far-field approximation and Fraunhofer diffraction valid. The sub-crystal elements must be small enough to treat the sound as plane waves [26]. In the diagram, the dash-dot line (denoted by t_c) connecting the scatterer and the centre of sub-crystal may represent a situation when the element is treated as a point source rather than a finite source. However, in reality, the element is finite and its response to ultrasound is characterised by the times t_1 and t_2. The effects of these t_c, t_1 and t_2 are collectively known as the "spatial impulse response (SIR)" [26]. The difference $|t_2 - t_1|$ determines the shape of the SIR and hence the shape of the waveform at the elements.

What we can do to simulate a dual-layered medium using Field-II, is to adjust the arrival time t_c in subplot (a) to match that from subplot (b), which is closer to the true scenario of a dual-layered medium when the reflection is ignored. However, we cannot change the difference $|t_2 - t_1|$ in (a) to match that in (b), since the lower-level sub-crystal calculation is not made available to Field-II users. The amount of potential error due to an inability to take into account the proper time difference may or may not be significant, but cannot be known unless we have our own means to simulate case (b).

3.1 Locally-developed dual-layer simulator

We have built an ultrasound simulator which is based on the concept of the SIR and is found to be compatible to Field-II when the speed of sound is uniform. The in-house ultrasound simulator has been further extended to take into account the beam behaviour in dual-layered media shown in Figure 3(b). In doing so, the refracted times t_1 and t_2 are individually calculated.

Figure 4 shows a comparison of simulated PSFs of dual-layered medium by delay adjustment of

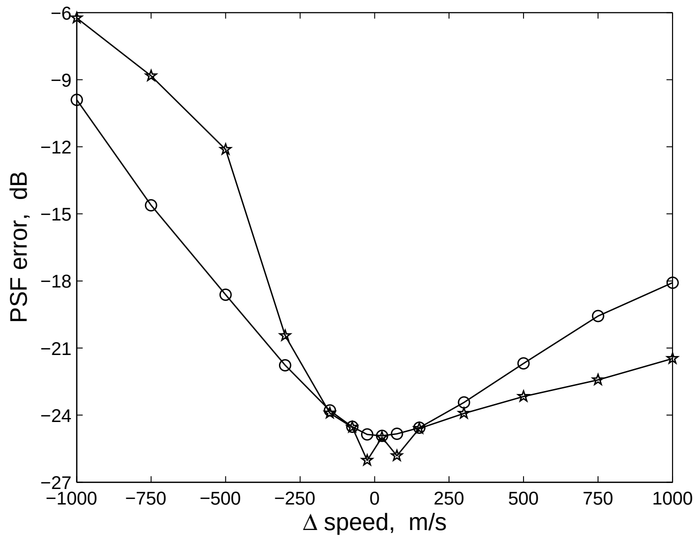

Figure 4: Comparison of simulated PSFs of dual-layered medium by delay modification of Field-II output and by our own simulator written for dual-layered medium. The curve with circular marks has the top-layer speed of 1540 m/s with different bottom-layer speeds. The curve with pentacles has different top-layer speeds but has the fixed bottom-layer speed of 1540 m/s. The speeds shown on the x-axis are all relative to 1540 m/s. The PSF error in decibel on the y-axis is difference between the two approaches.

Field-II output and by our own simulator written for dual-layered medium. The curve with circular marks has the top-layer speed of 1540 m/s with different bottom-layer speeds which are indicated in the x-axis. The curve with pentacles has different top-layer speeds but has a fixed bottom-layer speed of 1540 m/s. The speeds shown on the x-axis are all relative to 1540 m/s. The PSF error in decibels on the y-axis is the difference between the two methods. The trend is believed to be reasonable and systematic in the sense that the difference between the two approaches gets bigger as the sound-speed difference gets wider. The error levels recorded in this exercise ranges from -25 to -10 dB, but note that some of the tested speeds may be unrealistic. Such extreme speeds were evaluated to produce the overall trend of the difference between two approaches. For speed differences which are more realistic, the error level is less than -23 dB, which may be considered small.

4 Method and Simulations

We applied our sound-speed estimation technique to dual-layered two-dimensional simulated phantoms. The way the simulation was conducted is explained in this section. We start with examples illustrating how ultrasound images may behave when there is a layered change in the speed of sound.

4.1 Simulated reflectivity function

A two-dimensional imaginary phantom was created with five cysts whose geometry is shown in Figure 5. This five-cyst configuration corresponds to an echogenicity map characterised by macro-

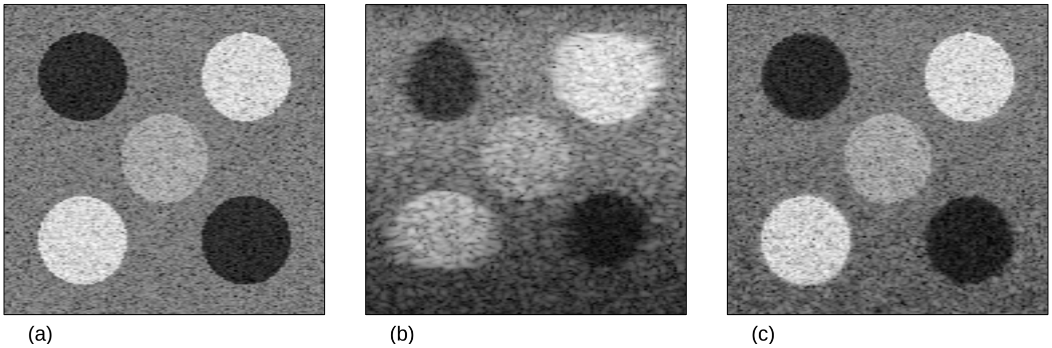

Figure 5: Behaviour of a dual-speed layered medium with the layer boundary at the centre of the middle cyst. (a) the simulated reflectivity function, (b) the simulated ultrasound image in which the speed of the top layer is 1540 m/s and that of the bottom layer is 250 m/s faster, and (c) the deconvolved image. B-mode images were drawn assuming the sound speed of 1540 m/s. The dynamic range of the logarithmically compressed images is 60 dB.

scopically smooth features. The reflectivity of each scatterer is then randomised by incorporating a Gaussian distribution which represents microscopic fluctuations. A reference image for the scatterer field is displayed in Figure 5(a).

4.2 Simulated ultrasound image formation

We blur the scatterer field by calculating a forward convolution of the image in Figure 5(a) with the PSF evaluated to have a dual-layered characteristic. The convolution algorithm itself is essentially the same as that used in the single-layered medium.

The dual-layered PSF is designed to have the layer boundary at the centre of the middle cyst. The speed of the top layer in the image (b) is 1540 m/s. The speed of the bottom layer is 1790 m/s. An excessive difference in speed was chosen to produce a clear demonstration of the dual-layer behaviour. Because the images are drawn assuming the speed to be 1540 m/s, the bottom layer in Figure 5(b) looks compressed because it takes less time for signals to arrive due to the faster speed. Later in Figure 6, it is also demonstrated that the bottom layer with slower speeds looks expanded because it takes more time for signals to arrive. It is also noted that there is no reflection appearing on the medium boundary in the ultrasound image, because this is not included in our model.

After blurring, zero-mean white Gaussian noise is added to the simulated ultrasound image. The signal-to-noise ratio after the addition of the noise is 40 dB. The image is demodulated to baseband, envelope detected and logarithmically compressed into 60 dB dynamic range. In Figure 5(b), we can easily identify the artefacts typically associated with ultrasound imaging. The axial depth of the lateral focus corresponds to the designed centre of the middle cyst. More serious blurring is easily spotted for scatterers away from the axial depth of the lateral focus. One can also notice the presence of coarse speckle in Figure 5(b).

4.3 Deconvolution via the correct sound speed

The blurred and noisy image in Figure 5(b) is restored using the algorithm in [20, 21], whose core structure is briefly outlined in Appendix A. It is noted that the deconvolution algorithm is identical to that used in the single-layered medium. The only difference lies in the PSF used in the deconvolution.

An example result of the deconvolution is shown in Figure 5(c). The restored image proves that the true geometry of the reflectivity function can be recovered after the deconvolution via the same PSF which was used to make the corresponding ultrasound image. A high degree of restoration is observed. The cysts appear again as circles with sharp boundaries. Furthermore, the speckle size is significantly reduced.

One may ask why the deconvolved result does not look perceptually the same as the designed reflectivity function despite the use of the same PSF for both forward and backward operations in the simulation. This is because of the presence of the additive Gaussian noise, and because of the blurring which involves loss of high frequency information and consequently causes the deblurring problem to be ill-posed.

4.4 Deconvolution via wrong sound speeds

In Figure 5(c), we have shown the deconvolution result conducted with the correct sound speed for the bottom layer. In addition, we have discovered that deconvolution with an incorrect speed results in different characteristics to those in the single-layer case. These new features are found to be important in determining the speed in the dual-layer scenario.

Figure 6 shows the deconvolution based on PSFs with various bottom-layer speeds. The simulated ultrasound image in subplot (a) was prepared to have the top-layer speed of 1540 m/s and that of the bottom layer 150 m/s slower. This is why the blurred cysts in the bottom layer are slightly elongated in the axial dimension compared to those in the top layer. The rest of the subplots from (b) to (f) illustrate deconvolution results using PSFs with various bottom-layer speeds. The speed of the top layer for these deconvolutions was maintained at 1540 m/s. The top-half images are properly restored in all the deconvolutions, as the exact speed information is used for the top layer. The bottom-half images are observed in various degrees of restoration.

It is clear that only the deconvolution with the correct speed in subplot (c) can restore the geometry of the bottom layer properly. The deconvolutions (subplots e and f) using bottom-layer speeds faster than that in the top-layer return the image with the bottom layer in varying degrees of axial expansion. This is because the deconvolution process is based on the assumption that the bottom-layer of the blurred ultrasound image in subplot (a) has already gone through the compression indicated by the faster bottom-layer speed of its PSF. Subsequently the deconvolution tries to correct the effect by elongation, which ends up causing further expansion than the ultrasound image in (a). In contrast, however, the deconvolutions (subplots b and c) that use slower speeds return images with a bottom layer further shrunk. This phenomenon can be explained similarly by reversed logic.

It is also noted that the black strip towards the bottom of image (b) is the result of an extreme compression through deconvolution. The corresponding information does not exist in the original ultrasound image (a) or in other words is outside the image size used in the deconvolution. The consequence of this additional axial compression or expansion after deconvolution is that the num-

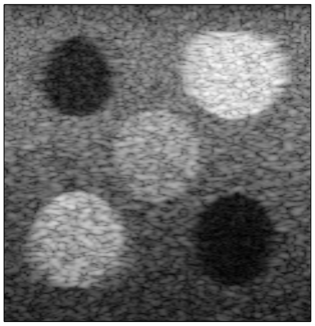

(a) Ultrasound image

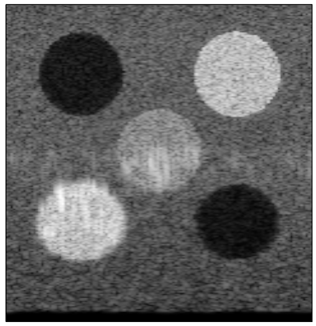

(b) Δ = -300 m/s

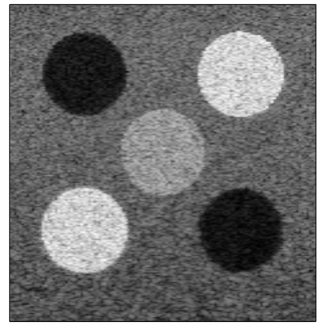

(c) Δ = -150 m/s

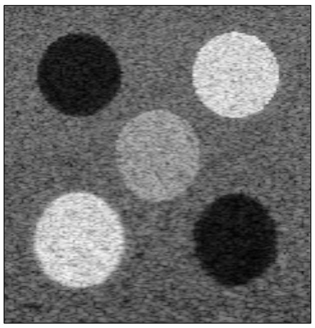

(d) $\Delta = 0$ m/s

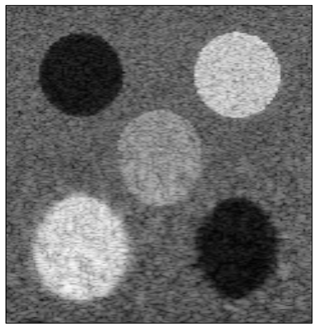

(e) $\Delta = +150$ m/s

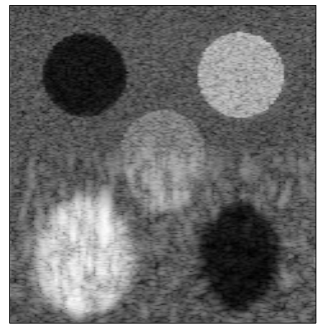

(f) $\Delta = +300$ m/s

Figure 6: Deconvolution images via various bottom-layer speeds with the layer boundary at the centre of the middle cyst. (a) Simulated ultrasound image, in which the speed of the top layer is 1540 m/s, and that of the bottom layer 150 m/s slower. (b)∽(f) Deconvolution via PSFs with various bottom-layer speeds. The label at each subplot denotes the speed of the bottom layer, which is relative to 1540 m/s, while that of the top layer was kept 1540 m/s. These B-mode images were drawn assuming the sound speed of 1540 m/s.

ber of horizontal lines are different, e.g., for given cysts in the bottom layers. This change may lead to a difficulty in picking up the inherent speed in the bottom layer, because so-called like-for-like comparison is not possible. The phenomenon is explained in Section 4.6.

At this point, readers may wonder why this extra feature does not occur in the case of single-layer soft tissue [17], in which the same approach of using various PSFs was essentially adopted. Example deconvolution images based on different speeds may be found in another publication of ours [22]. Unlike in dual-layered scenarios, in the single-layer deconvolution process it is not assumed that the bottom-half of the blurred images has already gone through either axial shrinkage or elongation compared to the top-half image. This is because speeds in both top- and bottom-half images are the same. Therefore, the deconvolution process is not designed to correct the potential change of scale in the axial dimension, but only carries out deblurring. This may be seen in Figure 6(d). Although the deconvolution image was actually prepared by the dual-layer algorithm, the case in Figure 6(d) is effectively a single-layered situation, since the top- and bottom-half speeds are identical. As seen, there is no further change in the aspect ratio of bottom-layer cysts from that in the original ultrasound image in Figure 6(a).

4.5 Uncertainty in PSF parameters

In order to estimate the speed of sound accurately and reliably, the other parameters required to build a PSF must be correct as well. Our research group has recently studied the effects of uncertainty in the PSF on non-blind deconvolution [22]. The parameters of an ultrasound imaging PSF have been systematically investigated. In total, six parameters were examined: uncertainty in the ultrasound machine was analysed by varying the axial depth of the lateral focus and the radius of elevational focus alongside the height and width of the transducer elements. Sensitivity to tissue influence was investigated by varying the speed of sound and frequency-dependent attenuation. We showed that these parameters could be assigned to certain families according to their characteristics. The speed of sound exhibited similar behaviour as the lateral focus for two-dimensional images. Therefore, the accuracy of the sound-speed estimation may be affected by that of the lateral focus. In our speed-estimation framework, what matters for the lateral focus is not how the focus is realised through soft tissues, but the intended delay profile applied to the imaging system which is not disturbed by the tissue. Because we know the delay profiles that were used, it is unlikely that our estimation of the sound speed is susceptible to uncertainty in the lateral focus.

4.6 Correlation metric

The overall strategy of our speed estimation method is to run multiple deconvolutions using PSFs with different speeds and to pick the speed which produces the best restoration. Therefore, a metric capable of determining the best outcome is as crucial as the non-blind deconvolution algorithm itself. In our previous publication [17], we have successfully used the following metric to determine the sound speed of single-layered media. Here, $\hat{\mathbf{x}}$ denotes the deconvolution image. The autocorrelation ($R_{\hat{\mathbf{x}}_i}[l]$) is calculated along the lateral line ($\hat{\mathbf{x}}_i$) at each i-th axial depth and then a summation ($\sum_l |R_{\hat{\mathbf{x}}_i}[l]|$) is made of the magnitude of all the l coefficients of the correlation. To produce a single-valued representation, another summation ($\sum_i \sum_l |R_{\hat{\mathbf{x}}_i}[l]|$) was taken of this value for all axial depths.

Figure 7 shows a graph of the aforementioned correlation metric for various speeds of sound in a simulated phantom. Several B-mode images of this data set have already been shown in Figure 6. The values of the correlation are normalised for display because the metric itself does not directly indicate a meaningful physical quantity but the relative differences are the most important. The top-half grey vertical line denotes the speed of the top layer, while the bottom-half black vertical line denotes the speed of the bottom layer. The dotted line with a full vertical length indicates the minimum of the correlation metric curve. Therefore, close alignment between the bottom-half black line and the full-length dotted line is expected when the correlation metric is capable of determining the correct speed for the bottom layer. This convention will be used in similar figures throughout the document. The speed values in Figure 7 are all relative to 1540 m/s. In this example, the graph indicates that the correlation metric has failed to identify the correct speed of sound for the bottom layer.

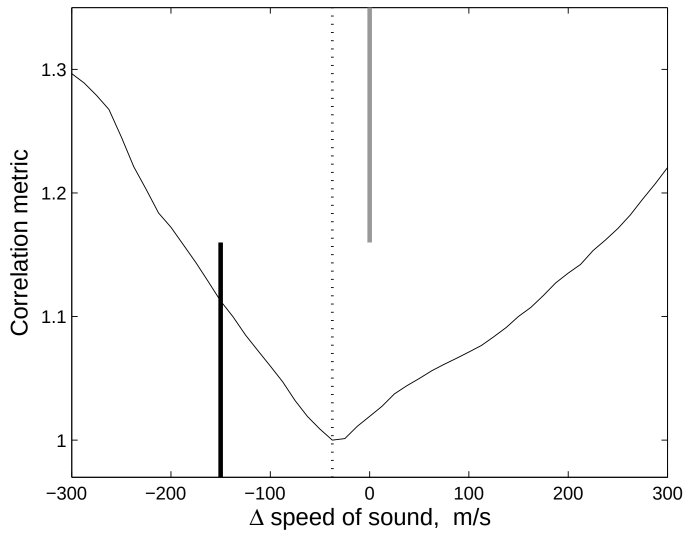

Figure 7: Plot of correlation metrics vs. various speeds of sound in a simulated dual-layered phantom. The correlation metric is normalised by its minimum for display purposes. The reference speed ($\Delta = 0$) is 1540 m/s. The top-half grey vertical line denotes the speed of the top layer, while the bottom-half black vertical line denotes the speed of the bottom layer. The dotted line with a full vertical length indicates the minimum of the correlation metric curve. For vertical lines, the y-axis values are irrelevant. This convention will be applied to similar other graphs.

4.7 Interpolation of deconvolution images

In previous sections, we have described changes in the axial dimensions of deconvolution results and the failure of the correlation metric. Because the correlation metric was successfully used for single-layered soft tissue [17] which does not incur the axial scale change, the cause of the failure is not likely to lie in the correlation metric itself, but perhaps in the extra change in the axial scale of deconvolution images. Such axial changes make the comparison of certain features, e.g., cysts inconsistent among deconvolutions, as they will have different numbers of horizontal lines inside them. Therefore, we have explored image interpolation strategies which make each feature intersect the same number of lines regardless of the bottom-layer speed used in the PSFs.

One-dimensional interpolation is conducted along each A-line in the bottom layer. The interpolation ratio at each speed is determined by the inverse of its speed: a lower speed will have more interpolated horizontal lines than a higher speed, and hence the procedure subsequently makes the deconvolution images of lower speeds expand and those of higher speeds contract. Readers may be able to imagine from Figure 6 that such interpolated images will have the same aspect ratio for different speeds. Figure 8 illustrates a typical example of the correlation metric applied to interpolated deconvolution images. The original data is the same as that in Figure 7. The correlation metric is now capable of detecting the correct speed of the bottom layer.

4.8 Cost of dual-layer PSFs

Each dual-layer PSF appearing in this article takes several hours to compute in Matlab regardless of whether it is done through adjusting outputs from Field-II or through the locally-developed

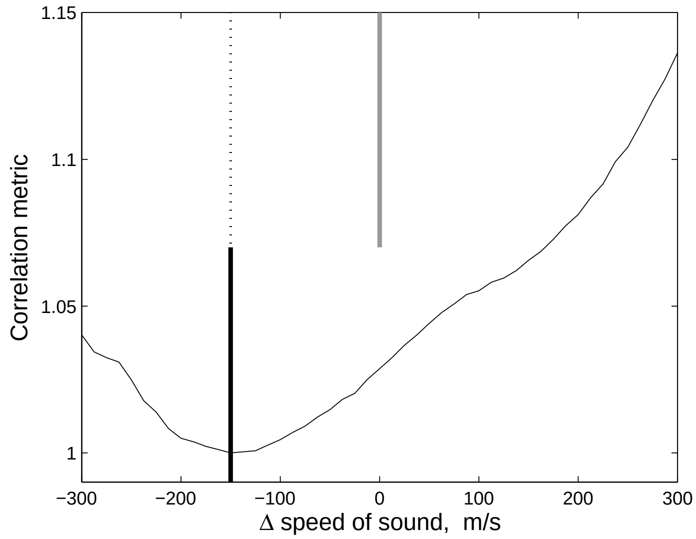

Figure 8: Plot of correlation metrics vs. various speeds of sound in a simulated dual-layered phantom. The deconvolution images were axially interpolated to make cysts occupy the same number of horizontal lines regardless of bottom-layer sound speeds in their PSFs.

ultrasound simulator. Field-II itself, whose core routines are compiled, usually runs quickly to produce a normal B-mode image. However the extra procedure of inter-element delay modification requires Field-II outputs in a raw format. For a high sampling rate, e.g., 66.67 MHz and transmit and receive element combination of 128 by 128, the Field-II module produces a large quantity of raw data that needs to be accessed several thousand times independently, and this is a costly operation.

This expensive nature of dual-layer operation makes it difficult to implement an optimisation strategy in searching for a minimum correlation, which was successfully adopted for a single-speed estimation [17]. Perhaps, the PSFs to produce the likes of Figure 8 can be run concurrently by using multiple computing resources, but the PSFs for an optimisation process can only be calculated in series. Because we are focusing in this article to demonstrate the speed-estimation capability of our deconvolution algorithm in dual-layered medium, we have not pursued such optimisation process, but analysed and displayed the correlation metric curves via numerous PSFs as illustrated in Figure 8.

5 *In vitro* measurements

After verifying our sound-speed estimation technique in the simulated dual-layered media, we proceeded to apply the estimation algorithm to *in vitro* dual-layered data sets.

The following ultrasound system was used to acquire the RF data for *in vitro* measurements. The system consisted of a General Electric[¶] probe RSP6-12 and a Diasus ultrasound machine from Dynamic Imaging Ltd. which has 128 A-line capability and operates an active aperture

[¶]GE Healthcare, Pollards Wood, Nightingales Lane, Chalfont St Giles, BUCKS UK of 32 piezoelectric elements[‖], synchronised with a Gage[**] Compuscope CS14200 digitiser. The digitisation process was linked to the locally-developed Stradwin software[††], which is a user-friendly cross-platform tool for medical ultrasound acquisition and visualisation.

5.1 Preparation of in-house phantoms

We locally produced ultrasound tissue-equivalent phantoms by mixing agar powder, scatterers, propanol and water [27]. For dual-layered phantoms with each layer having different speeds of sound, we created phantoms in two steps. First, a liquid form of phantom after heating and cooling of the aforementioned mixture is poured into an empty container, and was allowed to be congealed. Several hours later, when the phantom has completely solidified, another liquid form of phantom with different composition was poured into on top of the already solidified phantom. Subsequently the top layer was left to be solidified with the bottom layer. In this way, we prepared a pair of phantoms. One was made to have its top layer with thickness of 15.3 mm, and the other with 20.5 mm. The thickness of each top layer was evaluated later based on the estimated speeds of the top layer. The pair of phantoms were prepared such that the material in the top layer of one phantom is the same (and made together) as that in the bottom layer of the other phantom. For these in-house phantoms, the speed of sound in each layer is not known *a priori*. We measured their speeds by means of our deconvolution-based estimation method reported for a single-speed situation [17]: the speed measurement of the phantom material composing the top layer is a straightforward and direct implementation of the algorithm. Then, we treat the speed estimated for the top layer in one phantom as a golden standard for the speed to be estimated in the bottom layer of the other phantom through our dual-layer estimation algorithm.

5.2 Results of dual-layer algorithm applied to phantoms

Figures 9 and 10 illustrates examples of the correlation metric applied to these *in vitro* phantoms. For these data sets, the correlation metric is shown to detect the speeds of the bottom layer. The curve in Figure 9 demonstrates the uneven nature of the metric and indicates a potential risk if a local-minimum based search method is applied. This local fluctuation may be related to the interpolation process. Currently, there is no clear indication of which data set behaves better or worse after an axial interpolation is conducted. But, in general, they seem to detect the minimum with certain error bounds. More ultrasound acquisitions were carried out. For each phantom from the pair, a total of 8 measurements were conducted: 4 different lateral focus settings for 2 different locations in each phantom. The overall errors in the estimation of the bottom-layer speed were found to be:

-8.81 $\pm$ 15.62 m/s or -0.57 $\pm$ 1.01 % for the phantom in Figure 9;

+13.09 $\pm$ 16.72 m/s or +0.87 $\pm$ 1.12 % for the phantom in Figure 10.

Here the errors are presented in the notation of "mean $\pm$ standard deviation". The results are within or around 1 % range of errors.

The results suggest that the errors of the dual-layer estimation method are not as good as those accomplished for our single-speed estimation. We reported -0.44 $\pm$ 0.31 % for a phantom

[‖]Dynamic Imaging used to be based near Edinburgh in Scotland, but they are no longer in business.
[**]Gage, 900 N. State Street, Lockport IL 60441, USA
[††]This is available free at http://mi.eng.cam.ac.uk/~rwp/stradwin/ .

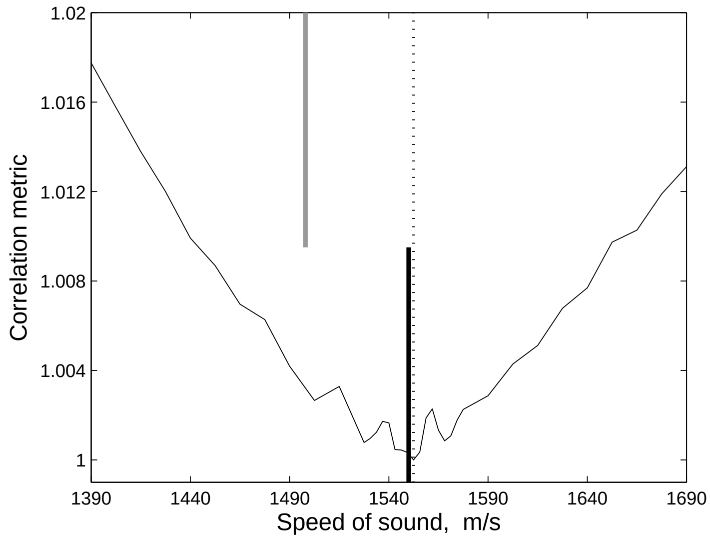

Figure 9: Plot of correlation metrics vs. various speeds of sound in an *in vitro* dual-layered phantom. The sound speeds are 1498 m/s in the top layer and 1550 m/s in the bottom layer, which are denoted by the top-half grey and the bottom-half black vertical lines, respectively. The error in the estimation of the bottom-layer speed is +2.5 m/s and is indicated by the full vertical-length dotted line.

made from an independent manufacturer and +0.01 ± 0.60 % for locally made phantoms [17]. Note especially that the standard deviation in the single-speed method is much better than that of the dual-speed method. This may indicate that the dual-speed approach could be inherently less reliable than that of the single speed. To reach an workable model within the framework of our deconvolution method [20, 21], several assumptions have been made in earlier sections: for example, trivial reflection from a layer boundary parallel to the probe aperture, perfect plane wave incidence and refraction guided by Snell's law, and phantoms with pure fluid characteristics. In addition, there may be an error propagated from the estimation of the top-layer speed whose bounds were mentioned earlier in this paragraph.

Despite the reduced performance of our dual-layer estimation algorithm compared to our single-speed method, it is discovered that our dual-layer approach is still capable of producing an estimate better than or comparable to some other methods reported for local speed estimation. Kondo et al. [4] reported the standard deviation of 41.1 m/s when the mean speed was 1550 m/s. Their method was developed for estimating the speed of local regions which is potentially more complicated than our dual-layer scenarios, but the quoted error was obtained from a single-speed homogeneous phantom consisted of agar and graphite particles. As a reminder, the standard deviation of our method for dual-layer phantoms is around 15 m/s. Ophir and Yazdi [5] measured the sound speed in the bottom layer of a dual-layered laboratory phantom using transaxial compression technique. They reported a mean estimation error of +0.75 % for the bottom-layer speed of a single phantom, while the standard deviation of error was not reported. Note that mean estimation errors for both of our *in vitro* phantoms are -0.57 and +0.87 %.

Figure 11 shows the ultrasound images for the phantom whose correlation metric is shown in Figure 10. The image (a) is the original ultrasound image acquired by the aforementioned

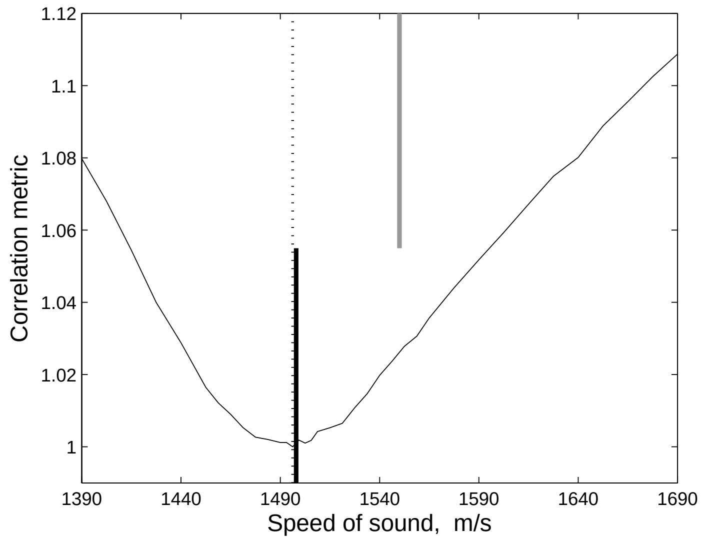

Figure 10: Plot of correlation metrics vs. various speeds of sound in an *in vitro* dual-layered phantom. The sound speeds are 1550 m/s in the top layer and 1498 m/s in the bottom layer, which are denoted by the top-half grey and the bottom-half black vertical lines, respectively. The error in the estimation of the bottom-layer speed is -1.75 m/s and is indicated by the full vertical-length dotted line.

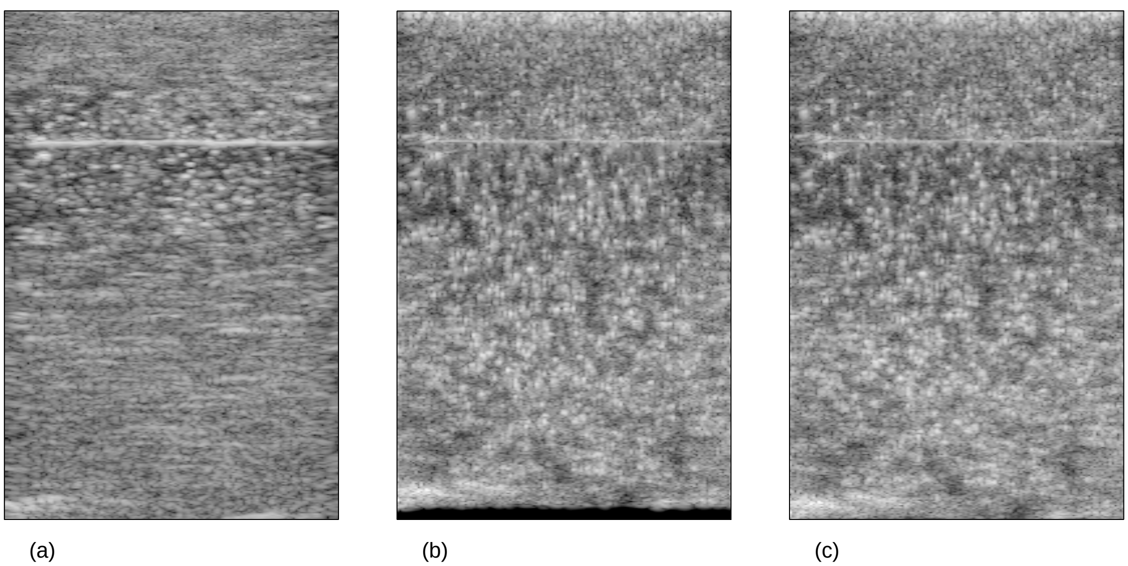

Figure 11: Ultrasound images of an *in vitro* in-house dual-layered phantom: (a) original ultrasound image, (b) deconvolution by dual-layered PSF with estimated speeds of 1550 m/s and 1496.25 m/s for the top- and bottom-layer, respectively, (c) deconvolution by single-layer PSF with a nominal speed of 1540 m/s. The bright horizontal lines are the boundary between two layers of phantom materials. The size of the images is 38.1 mm × 25.0 mm, when the speed of sound is assumed as 1540 m/s for comparison purposes. The ultrasound data set is the same as that used in Figure 10. The dynamic range of the logarithmically compressed images is 60 dB.

ultrasound system. The image (b) is the deconvolution via dual-layered PSF having estimated speeds of 1550 m/s and 1496.25 m/s for the top- and bottom-layer, respectively. The image (c) is the deconvolution by a single-layered PSF with nominal speed of 1540 m/s, which could be a usual choice of speed when there is no information available. The size of the images is 38.1 mm $\times$ 25.0 mm, when the speed of sound is assumed as 1540 m/s for comparison purposes. In images, one can see the bright horizontal lines which are indeed the boundary between the two layers of phantom material.

It is certain that both deconvolution results in images (b) and (c) are enhanced greatly from the original ultrasound image (a): the physical size of speckles are reduced, and point-like scatterers especially further down the images are restored to be more distinct from their surroundings. One can also notice that the boundary line gets thinner as a result of deblurring in deconvolution, which may indicate the amount of true reflection might not be as much as judged in the original image (a). An intriguing aspect about the boundary lines is that they seem to be tilted after deconvolution, but which appears to be an optical illusion upon closer inspection.

Unlike the stark perceptual difference between the original ultrasound image and two deconvolution results, it is hard to notice discrepancy between two deconvolution images in (b) and (c) except for the black strip. This is mainly because the speeds used for both PSFs are not very different. Such perceptual insensitivity was discussed in our previous publications [22, 17].

6 Conclusions

We have demonstrated that the image deconvolution applicable to medical ultrasound systems can be used to estimate the speed of sound in dual-layered media. It is assumed that pulse-echo ultrasound is mainly transmitted at the medium boundary. We have also developed an ultrasound simulator designed for layered media. In doing so, it has been discovered that for moderate speed differences the far-field diffraction of transducer elements in layered media is not significantly different from that obtained under the assumption of homogeneous media, although there is a systematic discrepancy in strict terms.

The speed of the top layer is estimated by the same deconvolution-based approach that we applied to homogeneous media. Once the top-layer speed is known, various PSFs for the dual-layered media with different candidate lower-layer speeds are constructed. Subsequently image deconvolutions are performed. The best restoration result is then determined through a correlation metric. It has also been found that unlike homogeneous media the deconvolution with dual-layered media requires axial interpolation for consistent comparison of correlation metrics among different speeds in the bottom layer.

Our estimation method for dual-layered media has been validated in simulations and *in vitro* phantoms. Its estimation errors were found to be -0.57 $\pm$ 1.01 % and +0.87 $\pm$ 1.12 % (mean $\pm$ standard deviation) for a pair of *in vitro* in-house phantoms. Its uncertainty level is not as good as that of our estimation approach for homogeneous media, but is found to be comparable to other local speed estimation methods.

7 Acknowledgements

The work was funded by the Engineering and Physical Sciences Research Council (reference EP/E007112/1) in the United Kingdom.

A Deconvolution Algorithm

The paper is mainly concerned with the estimation of the sound speed in pulse-echo ultrasound applications. But, the deconvolution of an ultrasound image is a pivotal part of our estimation process, and is also an important outcome. Therefore, we briefly recapitulate the key components of our deconvolution algorithm for the benefit of readers who may not be familiar with it. Complete details can be found in previous publications [20, 21].

A.1 Ultrasound image formation

The A-lines of an ultrasound imaging system can be mathematically modelled as a Fredholm integral of the first kind [20]. The wave propagation is assumed linear. Although non-linearity is present in *in vivo* scans of clinical applications, our approach is still applicable to ultrasound images when dominated by linearity. In medical ultrasound imaging, linearity is generally preserved in pulse propagation and reflection, with higher order harmonic imaging as exceptions [28]. When we adopt a discrete space-time formulation, the integral can be further simplified using a vector-matrix notation with a complex random variable $\mathbf{x}$ as the scatterer field (or reflectivity function) and $\mathbf{y}$ as the complex analytic baseband counterpart of the measured ultrasound signal:

$$\mathbf{y} = \mathbf{H}\,\mathbf{x} + \mathbf{n}\,. \tag{5}$$

Potential measurement errors are taken into account as complex additive white Gaussian noise ($\mathbf{n}$). $\mathbf{H}$ is a block diagonal matrix along the lateral and elevational dimensions. Each block matrix maps from the axial depth dimension to the time domain at a given lateral and elevational position. Here, multi-dimensional data ($\mathbf{y}, \mathbf{x}, \mathbf{n}$) are rearranged into one-dimensional equivalents by lexicographic ordering, and thus the sizes of the vectors and the matrix are: $N \times 1$ for $\mathbf{x}$, $\mathbf{n}$, and $\mathbf{y}$, and $N \times N$ for $\mathbf{H}$. Here, N is the total image size.

A.2 Deconvolution under an EM framework

Our goal is to estimate a scatterer field $\mathbf{x}$ from a noisy and blurred image $\mathbf{y}$. The algorithm operates in a Bayesian context. Because the finite resolution cell of a PSF merges the responses from neighbouring scatterers during the blurring process ($\mathbf{H}\,\mathbf{x}$), the deblurring procedure tends to be ill-posed, and therefore a direct inverse filtering is likely to fail. One of the standard solutions to this problem is to incorporate regularisation in a maximum *a posteriori* framework (MAP, see p.314 in [29]) with a prior on the scatterer field:

$$\hat{\mathbf{x}} = \arg\max_{\mathbf{x}} \left[\ln\, p(\mathbf{y} \mid \mathbf{x}, \sigma_n^2) + \ln\, p(\mathbf{x})\right]\,. \tag{6}$$

Here, $\hat{\mathbf{x}}$ is an estimate of the scatterer field, obtained from the deconvolution process, and σ_n^2 the variance of $\mathbf{n}$. Possible priors could involve assuming Gaussian or Laplacian statistics for the scatterer field. The Gaussian prior, in particular, leads to the well-known Wiener filter:

$$\hat{\mathbf{x}} = \arg \min_{\mathbf{x}} \left[\frac{1}{2\sigma_n^2} \|\mathbf{y} - \mathbf{H}\,\mathbf{x}\|^2 + \frac{1}{2} \mathbf{x}^H \mathbf{C}_x^{-1} \mathbf{x} \right] = (\mathbf{H}^H \mathbf{H} + \sigma_n^2 \mathbf{C}_x^{-1})^{-1} \mathbf{H}^H \mathbf{y} \ . \tag{7}$$

In a further simplified case of $\mathbf{C}_x = \sigma_x^2 \mathbf{I}_N$, this is known as zero-order Tikhonov regularisation. The superscript H denotes the Hermitian transpose. The term $\mathbf{C}_x$ represents the covariance matrix $\mathbf{E}(\mathbf{x}\mathbf{x}^H)$ of the complex random variable $\mathbf{x}$, σ_x^2 the variance of $\mathbf{x}$, and $\mathbf{I}_N$ the identity matrix with size N. Instead of using this conventional prior for the entire tissue ($\mathbf{x}$), we model the tissue reflectivity as the product of microscopically randomised fluctuations ($\mathbf{w}$) and a macroscopically smooth tissue-type image called the echogenicity map ($\mathbf{S}$) which shares the characteristics of natural images [21]:

$$\mathbf{x} = \mathbf{S}\,\mathbf{w} \ . \tag{8}$$

Here, $\mathbf{w}$ is a $N \times 1$ complex vector, and $\mathbf{S}$ is a $N \times N$ diagonal matrix with real non-negative values.

If a zero-mean Gaussian prior is assigned to $\mathbf{w}$, then $\mathbf{x}$ is also observed to be a zero-mean Gaussian when $\mathbf{S}$ is known. It leads to the conditional probability density function of $\mathbf{x}$, given $\mathbf{S}$:

$$p(\mathbf{x} \mid \mathbf{S}) \propto \frac{1}{|\mathbf{S}|^2} \exp\left(-\frac{1}{2} \mathbf{x}^H \mathbf{S}^{-2} \mathbf{x} \right) \ . \tag{9}$$

This implies two key procedures of our algorithm. First, when $\mathbf{S}$ is known, then $\mathbf{x}$ can be found using the Wiener filter (Equation 7) with $\mathbf{S}^2$ representing the covariance matrix. Second, when $\mathbf{x}$ is known from the first step and $\ln |w_i|$ is treated as additive noise, then $\mathbf{S}$ can be determined through a denoising process:

$$\ln S_i = \ln |x_i| - \ln |w_i| \ , \qquad i = 1, \cdots, N \ . \tag{10}$$

The subscript i denotes the element of the vectors and the diagonal matrix, and $|\cdot|$ the modulus of a complex variable. Using an expectation-maximisation (EM, see p.285 in [29]) framework, we can construct an iterative deconvolution strategy alternating between the Wiener filter for $\mathbf{x}$ and the denoising for $\mathbf{S}$.

For denoising, we adopted a wavelet-based algorithm to separate $\mathbf{x}$ into its $\mathbf{S}$ and $\mathbf{w}$ components. We therefore represent the reflectivity function ($\mathbf{x}$) using the dual-tree complex wavelet transform DT-$\mathbb{C}$WT [30, 31] which has been shown to be particularly effective in denoising applications [32].

References

[1] Anderson, M. E., McKeag, M. S., and Trahey, G. E., "The impact of sound speed errors on medical ultrasound imaging," *Journal of the Acoustical Society of America*, Vol. 107, No. 6, June 2000, pp. 3540–3548.

[2] Hayashi, N., Tamaki, N., Senda, M., Yamamoto, K., Yonekura, Y., Torizuka, K., Ogawa, T., Katakuraand, K., Umemura, C., and Kodama, M., "A New Method of Measuring In Vivo Sound Speed in the Reflection Mode," *Journal of Clinical Ultrasound*, Vol. 16, No. 2, 1988, pp. 87–93.

[3] Robinson, D. E., Ophir, J., Wilson, L. S., and Chen, C. F., "Pulse-echo ultrasound speed measurements: progress and prospects," *Ultrasound in Medicine & Biology*, Vol. 17, No. 6, 1991, pp. 633–646.

[4] Kondo, M., Takamizawa, K., Hirama, M., Okazaki, K., Iinuma, K., and Takehara, Y., "An evaluation of an in vivo local sound speed estimation technique by the crossed beam method," *Ultrasound in Medicine & Biology*, Vol. 16, No. 1, 1990, pp. 65–72.

[5] Ophir, J. and Yazdi, Y., "A transaxial compression technique (TACT) for localized pulse-echo estimation of sound speed in biological tissues," *Ultrasonic Imaging*, Vol. 12, 1990, pp. 35–46.

[6] Saijo, Y., Filho, E. S., Sasaki, H., Yambe, T., Tanaka, M., Hozumi, N., Kobayashi, K., and Okada, N., "Ultrasonic Tissue Characterization of Atherosclerosis by a Speed-of-Sound Microscanning System," *IEEE Transactions on Ultrasonics, Ferroelectrics, and Frequency Control*, Vol. 54, No. 8, 2007, pp. 1571–1577.

[7] Chenevert, T. L., Bylski, D. I., Carson, P. L., Meyer, C. R., Bland, P. H., Adler, D. D., and Schmitt, R. M., "Ultrasonic Computed Tomography of the Breast," *Radiology*, Vol. 152, 1984, pp. 155–159.

[8] André, M. P., Janée, H. S., Martin, P. J., Otto, G. P., Spivey, B. A., and Palmer, D. A., "High-Speed Data Acquisition in a Diffraction Tomography System Employing Large-Scale Toroidal Arrays," *International Journal of Imaging Systems and Technology*, Vol. 8, No. 1, 1997, pp. 137–147.

[9] Duric, N., Littrup, P., Rama, O., and Holsapple, E., "Computerized ultrasound risk evaluation (CURE): first clinical results," *Acoustical Imaging*, edited by M. P. André, the 28th International Symposium on Acoustical Imaging, Springer, March 2005, pp. 173–181.

[10] Wiskin, J., Borup, D. T., Johnson, S. A., Berggren, M., Abbott, T., and Hanover, R., "Full-wave, non-linear, inverse scattering: high resolution quantitative breast tissue tomography," *Acoustical Imaging*, edited by M. P. André, the 28th International Symposium on Acoustical Imaging, Springer, March 2005, pp. 183–193.

[11] André, M. P., Barker, C. H., Sekhon, N., Wiskin, J., Borup, D., and Callahan, K., "Pre-clinical Experience with Full-Wave Inverse-Scattering for Breast Imaging: Sound Speed Sensitivity," *Acoustical Imaging*, edited by I. Akiyama, the 29th International Symposium on Acoustical Imaging, Springer, Shonan, Japan, April 2007, pp. 73–80.

[12] Anderson, M. E. and Trahey, G. E., "The direct estimation of sound speed using pulse-echo ultrasound," *Journal of the Acoustical Society of America*, Vol. 104, No. 5, November 1998, pp. 3099–3106.

[13] Flax, S. W. and O'Donnell, M., "Phase-Aberration Correction Using Signals From Point Reflectors and Diffuse Scatterers: Basic Principles," *IEEE Transactions on Ultrasonics, Ferroelectrics, and Frequency Control*, Vol. 35, No. 6, November 1988, pp. 758–767.

[14] Nock, L., Trahey, G. E., and Smith, S. W., "Phase aberration correction in medical ultrasound using speckle brightness as a quality factor," *Journal of the Acoustical Society of America*, Vol. 85, No. 5, May 1989, pp. 1819–1833.

[15] Ng, G. C., Freiburger, P. D., Walker, W. F., and Trahey, G. E., "A Speckle Target Adaptive Imaging Technique in the Presence of Distributed Aberrations," *IEEE Transactions on Ultrasonics, Ferroelectrics, and Frequency Control*, Vol. 44, No. 1, January 1997, pp. 140–151.

[16] Ng, G. C., Worrell, S. S., Freiburger, P. D., and Trahey, G. E., "A Comparative Evaluation of Several Algorithms for Phase Aberration Correction," *IEEE Transactions on Ultrasonics, Ferroelectrics, and Frequency Control*, Vol. 41, No. 5, September 1994, pp. 631–643.

[17] Shin, H.-C., Prager, R., Gomersall, H., Kingsbury, N., Treece, G., and Gee, A., "Estimation of Speed of Sound using Medical Ultrasound Image Deconvolution," Tech. Rep. CUED/F-INFENG/TR626, Cambridge University Engineering Department, 2009.

[18] Napolitano, D., Chou, C.-H., McLaughlin, G., Ji, T.-L., Mo, L., DeBusschere, D., and Steins, R., "Sound speed correction in ultrasound imaging," *Ultrasonics*, Vol. 44, 2006, pp. e43–e46.

[19] Richter, K. and Heywang-Köbrunner, S. H., "Sonographic Differentiation of Benign from Malignant Breast Lesions: Value of Indirect Measurement of Ultrasound Velocity," *American Journal of Roentgenology*, Vol. 165, No. 4, 1995, pp. 825–831.

[20] Ng, J., Prager, R., Kingsbury, N., Treece, G., and Gee, A., "Modeling Ultrasound Imaging as a Linear Shift-Variant System," *IEEE Transactions on Ultrasonics, Ferroelectrics, and Frequency Control*, Vol. 53, No. 3, March 2006, pp. 549–563.

[21] Ng, J., Prager, R., Kingsbury, N., Treece, G., and Gee, A., "Wavelet Restoration of Medical Pulse-Echo Ultrasound Images in an EM framework," *IEEE Transactions on Ultrasonics, Ferroelectrics, and Frequency Control*, Vol. 54, No. 3, March 2007, pp. 550–568.

[22] Shin, H.-C., Prager, R., Ng, J., Gomersall, H., Kingsbury, N., Treece, G., and Gee, A., "Sensitivity to point-spread function parameters in medical ultrasound image deconvolution," *Ultrasonics*, Vol. 49, 2009, pp. 344–357.

[23] Jensen, J., "Field: A Program for Simulating Ultrasound Systems," *Medical* & *Biological Engineering* & *Computing*, Vol. 34, 1996, pp. 351–353.

[24] Kinsler, L. E., Frey, A. R., Coppens, A. B., and Sanders, J. V., *Fundamentals of Acoustics*, John Wiley & Sons, New York, 3rd ed., 1982.

[25] Angelsen, B. A. J., *Ultrasound Imaging: Waves, Signals, and Signal Processing*, Vol. I, Emantec AS, Trondheim, Norway, 2000.

[26] Jensen, J. and Svendsen, N. B., "Calculation of pressure fields from arbitrarily shaped, apodized, and excited ultrasound transducers," *IEEE Transactions on Ultrasonics, Ferroelectrics, and Frequency Control*, Vol. 39, 1992, pp. 262–267.

[27] Burlew, M. M., Madsen, E. L., Zagzebski, J. A., Banjavic, R. A., and Sum, S. W., "A New Ultrasound Tissue-Equivalent Material," *Radiation Physics*, Vol. 134, March 1980, pp. 517–520.

[28] Taxt, T., "Three-Dimensional Blind Deconvolution of Ultrasound Images," *IEEE Transactions on Ultrasonics, Ferroelectrics, and Frequency Control*, Vol. 48, No. 4, July 2001, pp. 867–871.

[29] Therrien, C. W., *Discrete Random Signals and Statistical Signal Processing*, Prentice Hall, Inc, Englewood Ciffs, NJ, USA, 1992.

[30] Kingsbury, N., "Image processing with complex wavelets," *Philosophical Transactions of The Royal Society of London Series A*, Vol. 357, 1999, pp. 2543–2560.

[31] Kingsbury, N., "Complex wavelets for shift invariant analysis and filtering of signals," *Applied and Computational Harmonic Analysis*, Vol. 10, 2001, pp. 234–253.

[32] Sendur, L. and Selesnick, I. W., "Bivariate Shrinkage Functions for Wavelet-Based Denoising Exploiting Interscale Dependency," *IEEE Transactions on Signal Processing*, Vol. 50, No. 11, 2002, pp. 2744–2756.